Atomically engineered interfaces yield extraordinary electrostriction

Zhang, Haiwu; Pryds, Nini; Park, Dae-Sung; Gauquelin, Nicolas; Santucci, Simone; Christensen, Dennis V.; Jannis, Daen; Chezganov, Dmitry; Rata, Diana A.; Insinga, Andrea R.

Total number of authors:
16

Published in:
Nature

Link to article, DOI:
10.1038/s41586-022-05073-6

Publication date:
2022

Document Version
Early version, also known as pre-print

Atomically engineered interfaces yield extraordinary electrostriction

Haiwu Zhang[1,7*], Nini Pryds[1,7*], Dae-Sung Park[2], Nicolas Gauquelin[3], Simone Santucci[1], Dennis V. Christensen[1], Daen Jannis[3], Dmitry Chezganov[3], Diana A. Rata[4], Ivano E. Castelli[1], Johan Verbeeck[3], Igor Lubomirsky[5], Paul Muralt[6], Dragan Damjanovic[2], and Vincenzo Esposito[1*]

[1]Department of Energy Conversion and Storage, Technical University of Denmark, Fysikvej 309, 2800 Kgs. Lyngby, Denmark

[2]Group for Ferroelectrics and Functional Oxides, Department of Materials Science, Swiss Federal Institute of Technology-EPFL, CH-1015 Lausanne, Switzerland

[3]Electron Microscopy for Materials Science (EMAT), University of Antwerp, B-2020 Antwerpen, Belgium

[4]Institut für Physik, Martin-Luther-Universität Halle-Wittenberg, 06120 Halle, Germany

[5]Department of Materials and Interfaces, Weizmann Institute of Science, Rehovot 76100, Israel

[6]Department of Materials, Swiss Federal Institute of Technology, 1015, Switzerland

[7] These authors contributed equally: H. Zhang, N. Pryds

*e-mail: haizh@dtu.dk; nipr@dtu.dk; vies@dtu.dk

Electrostriction is a property of all the dielectric materials where an applied electric field induces a mechanical deformation proportional to the square of the electric field. The magnitude of the effect is usually minuscule. However, recent discoveries of symmetry-breaking phenomena at interfaces opens up the possibility to extend the electrostrictive response to a broader family of dielectric materials.[1,2] Here, we engineer the electrostrictive effect by epitaxially depositing alternating layers of

Gd_2O_3-doped CeO_2 and Er_2O_3-stabilized δ-Bi_2O_3 with atomically controlled interfaces on $NdGaO_3$ substrates. We find that the electrostriction coefficient reaches 2.38×10^{-14} m^2/V^2, exceeding the best-known relaxor ferroelectrics by three orders of magnitude. Our atomic-scale calculations show that the extraordinary electrostriction coefficient is driven by the coherent strain imparted by the interfacial lattice mismatches. Thus, artificial heterostructures open a new avenue to design and manipulate electrostrictive materials and devices for nano/micro actuation and cutting-edge sensor applications.

Materials developing strain in response to an electric field have attracted significant attention over the previous several decades due to their wide applications, ranging from non-resonant actuators, high-end transducers, artificial muscles, energy harvesting, and various sensors.[3-4] While piezoelectricity is limited to materials with a non-centrosymmetric crystal structure, electrostriction is a general property of all dielectrics, which produces a high displacement accuracy with the absence of strain-field hysteresis and remnant polarization. However, the electrostriction coefficient (M_{xx}) is usually low, attaining a value less than 10^{-19} m^2/V^2 for simple oxides such as MgO, TiO_2 and Y:ZrO_2.[5] Owing to their very high electromechanical responses, the two archetypes of electrostrictive materials are relaxor ferroelectrics and ferroelectric polymers.[5, 6] The former generates a significant electrostriction coefficient of 1.0×10^{-17} m^2/V^2 with mechanical stress of 150 MPa or less.[7, 8] In contrast, flexible polymers exhibit high

electrostrictive coefficients up to 1.8×10^{-18} m^2/V^2 while the stress delivered is about two orders of magnitude lower (2 MPa on average).[9]

A new family of high-performance electrostriction materials was recently discovered in Gd_2O_3-doped CeO_2 (CGO), exhibiting anomalously large electrostriction with the maximum stress exceeding 500 MPa.[10,11] The investigated CGO-based films have typically large thicknesses (t > 300 nm), where the in-plane biaxial strain is fully relaxed, and the M_{xx} is improved by less than one order of magnitude compared to the bulk counterparts, i.e., 10^{-17} *vs* 10^{-18} m^2V^{-2}.[10, 13-15]

Over the past decade, increased interest has been placed in the growth of ultrathin complex oxide heterostructures. These films exhibit superior properties, such as fast ionic conduction,[16] metal-to-insulator transition,[17] and ferroelectricity in otherwise paraelectric materials.[18] Such emergent properties are associated with the complex yet tailorable interfacial morphology that gives rise to ionic/electronic redistribution, symmetry breaking and strain gradients.[1,2] For ferroelectric thin films, the evolution of electric polarization with reduced film thickness has been one of the crucial topics in the field, with interfaces and surfaces playing a pivotal role.[19-23] However, to date, the effects of interfaces and synthesis of ultrathin films (<< 100 nm) on the electrostriction property has not been explored.

Here, we demonstrate a new concept of engineering electrostriction through artificial interfaces. We selected Gd_2O_3-doped CeO_2 (CGO) and Er_2O_3-stabilized δ-Bi_2O_3 (ESB) as the two model material systems. We designed the multilayers to achieve two purposes: 1) to establish an interfacial configuration where the lattice mismatch can be used as a tuning knob and 2) to confine the electrostrictive layers by selecting a set of two materials that develop desired lattice distortions under an electric field. With this strategy, we achieved an electrostrictive enhancement of three orders of magnitude when compared to thick CGO films, reaching the highest value (M_{xx} ~10^{-14} m^2/V^2) measured so far in any electrostrictive material. This artificial electrostrictive heterostructure paves a new way for achieving extraordinary electrostriction, yielding new opportunities for nano/micro electrostrictive devices.

Ultrathin films were deposited by pulsed laser deposition (PLD). The heterostructures consist of alternating layers of gadolinium-doped ceria ($Ce_{0.8}Gd_{0.2}O_{1.9}$, CGO) and erbium-stabilized bismuth oxide ($Er_{0.4}Bi_{1.6}O_3$, ESB) deposited on pseudocubic (pc) [010]-oriented $NdGaO_3$ substrates (NGO). The heterostructures are defined as NGO/CGO/$[ESB/CGO]_N$, where N = {1, 3, 7, 10, 15} is the number of [ESB/CGO] bilayers as schematically illustrated in Fig. 1a. The total thickness of the thin films was fixed at about 17 nm with a ratio of 1:1 of CGO and ESB. We define a modulation length

(Λ) as the thickness of the [ESB/CGO] bilayers with values of 8.5, 2.8, 1.2, 0.9 and 0.6 nm, corresponding to N = 1, 3, 7, 10 and 15, respectively. High-angle annular dark-field scanning transmission electron microscopy (HAADF-STEM) *Z*-contrast images of NGO/CGO/[ESB/CGO]$_7$ reveal the epitaxial relationship between the constituent layers, with ESB exhibiting a brighter ADF image contrast than CGO (Fig. 1b). Atomically resolved EDX profiles of Ce, Er and O show the compositional variation from which well-defined interfaces can be identified. Up to a value of N = 7 and Λ = 1.2 nm, we observe no sign of dopant segregation or formation of extended defects (e.g. dislocations or line defects). However, a further increase of N to 10 (Λ=0.9 nm) results in significant chemical intermixing, indicating the collapse of the heterostructure (Extended Data Fig. 1).

The electrostrictive response of the 17 nm thick multilayer deposited on an NGO cantilever is proportional to the square of the electric field strength (Extended Data Fig. 2). The maximum stress generated in this configuration was 9.7 GPa. Fig. 1c shows the electrostriction coefficient (M_{xx}) of the multilayers as a function of the modulation length measured at 1 Hz. For ease of comparison, the electrostriction coefficients (M_{xx}) of a single layer of CGO thin film (t = 17 nm) deposited on NGO are also shown, as well as a range of thick CGO films ($t \geq 400$ nm) deposited on different substrates taken from the literature.[10,14,15] Comparisons with Bi_2O_3-based films are not included as their

104 electrostrictive properties have not been investigated due to their structural and chemical
105 instabilities.[11, 24, 25] As seen in Fig. 1c, the measured electrostriction coefficients exhibit a
106 "volcano-like" shape as a function of the modulation length, reaching a maximum at N =
107 7 (Λ = 1.2 nm). The electrostriction coefficients generally follow a linear increase as the
108 modulation length decreases down to 1.2 nm. Different materials' values reported in the
109 literature follow the same trend, regardless of the deposition methods, process parameters,
110 microstructure of the films and type of substrate/electrode.[10, 14, 15, 26] Remarkably, for the
111 first time, we show that the maximum M_{xx} of the heterostructure (2.38×10^{-14} m^2/V^2)
112 surpasses that of the thick CGO films by more than three orders of magnitude.[10, 14, 15, 26]
113 However, as Λ decreases below Λ = 1.2 nm (N > 7) the electrostriction coefficient
114 decreases significantly. This effect relates to intermixing at the interfaces (Extended Data
115 Fig. 1) and the corresponding decrease in the electrostrictive performance.
116
117 We have systematically investigated the performance of the heterostructures with
118 different stacking sequences where the deposition on NGO was started with either CGO
119 or ESB. When ESB was deposited directly on NGO (NGO/ESB/$[CGO/ESB]_7$), the
120 heterostructure is unstable and shows a reduced electrostriction coefficient of 3.0×10^{-16}
121 m^2/V^2 (Extended Data Fig. 3). In contrast, when CGO was deposited on NGO
122 (NGO/CGO/$[ESB/CGO]_7$), the heterostructure was stable and exhibited a significantly
123 enhanced electrostriction, highlighting the importance of the stacking sequence. We thus

used NGO/CGO/[ESB/CGO]$_N$ as the main configuration in our experiments, ensuring that the heterostructure is capped with CGO to avoid degradation of the ESB. Fig. 1d shows the electrostriction coefficient, M_{xx}, for heterostructures with $N = 1$ ($\Lambda = 12.0$ nm), $N = 7$ ($\Lambda = 1.21$ nm) and $N = 15$ ($\Lambda = 0.57$ nm) as a function of the frequency. Our results outperformed any known electrostrictive materials, including bulk CGO,[26] Y/Nb:Bi_2O_3,[11] $La_2Mo_2O_9$,[27] Y:ZrO_2 (YSZ)[11] as well as the commercial relaxor ferroelectrics, such as $Pb(Mg_{1/3}Nb_{2/3})O_3$-$PbTiO_3$ (PMN-PT),[6] P(VDF-TrFE) copolymers[9] and the recently discovered ultrahigh electrostriction in lead halide perovskites.[28] Similar to bulk CGO, the electrostriction coefficient of the heterostructures decreases when the frequency is increased ($1 < f < 200$ Hz). The measured M_{xx} decreases from 2.38×10^{-14} at 1 Hz to 3.76×10^{-15} m^2/V^2 at 200 Hz for $N = 7$. The enhancement in the electrostrictive response may lead to novel applications, as it permits a significant decrease in the operating electrical field, which improves the long-term stability of the devices.

One potential drawback associated with multilayers is the possible delamination at the interfaces after cyclic electrical loading, leading to the failure of the electrostrictive devices. Therefore, we have evaluated the fatigue behaviour of NGO/CGO/[ESB/CGO]$_7$ as a function of time at a constant electric field of 17.4 kV cm^{-1}. The field-induced stress shows no sign of degradation and remains stable after 1000 cycles at 1 Hz. Subsequent

143 measurements further confirm the mechanical stability at 50 and 200 Hz for another 1000
144 cycles, respectively (Extended Data Fig. 4).
145
146 We have performed structural analysis to rationalize the exceptionally large
147 electrostriction coefficients. Fig. 2a shows the reciprocal space mappings (RSMs) around
148 the asymmetric $(221)_{pc}$ reflection of NGO for different heterostructures with different *N*.
149 The out-of-plane position and shape of the (420) reflections of the heterostructures change
150 with increasing *N*. The overall structural coherency is essentially maintained, indicating
151 that the in-plane lattice parameters of the heterostructure are coherent with respect to the
152 substrate, which is in line with the STEM results. The sub-peaks along (110) observed
153 for $N = 1$, and 3 and along the (004) are attributed to the lattice relaxations within the
154 CGO and ESB layer. X-ray diffraction (2θ-ω scan) analysis reveals that the
155 heterostructures are phase-pure films oriented along the (110) crystallographic direction
156 (Fig. 2b). A minor signal of (111) orientation is observed for the $N = 3$, 7 and 15 (results
157 are not shown here). The Laue diffraction oscillations around the superlattice peaks
158 originate from the coherency between individual sublayers and indicate smooth interfaces
159 between the ESB and CGO layers (Fig. 2b), aligning well with the STEM results (Fig.
160 1b). To accommodate the significant mismatch and allow cube-on-cube growth, the
161 fluorite oxide (CGO) grows epitaxially on the perovskite oxide (NGO) by allowing a
162 rotation of 45°. This arrangement results in an epitaxial relationship of

163 $<110>_{CGO}//<010>_{pc\ NGO}$ (see also Extended Data Fig. 1a) and a significant decrease in the
164 mismatch to ~ 1% (See Fig. 2c).
165
166 For the heterostructure (NGO/CGO/$[ESB/CGO]_N$), the lattice mismatch to the substrate
167 is entirely compensated by elastic strain, generating an average in-plane strain of 1% (see
168 Fig. 2d). On the other hand, the magnitude of the average out-of-plane strain decreases
169 when increasing N from 1 to 7. The minimum strain value is observed at $1/\Lambda = 0.8$ nm^{-1}
170 with the abnormal strain change for $1/\Lambda > 0.8$ nm^{-1} attributed to the chemical intermixing
171 at the interfaces, as shown in the EELS and EDX maps in Extended Data Fig. 1b and c.
172 The minimum in the out-of-plane lattice parameters at $1/\Lambda = 0.8$ nm^{-1} correlates well with
173 the measured modulation length-dependent electrostriction coefficient (Fig. 1c).
174
175 We next performed atomic-scale simulations on CGO/ESB heterostructures to understand
176 the structural evolution as a function of modulation length (Fig. 2). The model structures
177 are optimized with the in-plane lattice parameters fixed to the NGO substrate, while the
178 out-of-plane lattice parameter is allowed to relax. The calculations were carried out for
179 alternating layers of CGO and ESB with different modulation lengths, corresponding to
180 96, 48, 32, 24, 16, 12, 8, 6 and 4 cationic planes, respectively (see Method section). Fig.
181 3a is a schematic illustration of the modulation length, and the definition of the cationic
182 interplanar distance (d_C) projected onto the out-of-plane direction. The amplitude of

CGO/ESB interfacial coupling is captured by the variation of d_C as a function of modulation length (Fig. 3b). For example, for Λ = 18.56 nm (96 cationic planes), the lattice relaxation yields two distinct plateaus at 1.92 and 1.96 Å, close to the individual interplanar distances of bulk CGO and ESB, respectively. This range of values agrees well with the lattice relaxation observed for N = 1 and N = 3 in the RSMs shown in Fig. 2a.

With the decrease of Λ, the interfacial coupling becomes progressively evident. By further reducing Λ towards 1.55 nm and beyond (approaching the modulation length of 1.2 nm for NGO/CGO[ESB/CGO]$_7$), the interplanar distances become gradually frustrated. At Λ = 0.78 Å, the discrimination between the interfaces and individual regions becomes difficult. The structural evolution is also associated with a peak maximum ($1/\Lambda$ = 0.8 nm^{-1}) in the out-of-plane lattice parameter in which above the modulation length decreases as shown in Fig. 3c. Remarkably, the results obtained from the atomic-scale simulations agrees well with the results obtained from the X-ray diffractions and the electrostrictive measurements (Fig. 1c). The above results reveal a clear correlation between the electromechanical properties and the epitaxial strain.

To further understand the relationship between the electromechanical properties, the modulation length and strain, we perform molecular dynamics (MD) simulations on heterostructures with different modulation lengths and biaxial strain (ε*). Fig. 4a shows

the calculated Helmholtz free energy (F) as a function of the biaxial strain for the heterostructure with Λ = 1.55 nm (12 cationic layers), which is close to the maximum electrostrictive effect (Fig. 1c). The system has the lowest total energy (F) in the absence of strain and increasing free energy when compressive or tensile strains are applied. The free energy increases at a specific strain value and exhibits a maximum function of $1/\Lambda$ (Fig. 4b). This effect is attributed to the enhanced interlayer interactions, as CGO and ESB couple at the interfaces.

Applying an electrical field of E = 20 kV/cm along the $+x$ direction causes an energy difference $\Delta F = F_{E = 20\ kV/cm} - F_{E = 0}$, which is shown in Fig. 4c as a function of Λ and different ε*. Interestingly, ΔF has a parabolic behaviour as a function of $1/\Lambda$, indicating a linear relationship between ΔF and $(1/\Lambda)^2$. Assuming that the in-plane and out-of-plane lattice parameters are allowed to relax, the energy change, ΔF, will be dominated by the elastic energy due to the strain developed (Δu). Thus, ΔF relates to Δu following Hooke's law: $\Delta F \propto (\Delta u)^2$. Since the electrostriction coefficient M_{xx} is directly proportional to Δu, one could derive the following relationship $(M_{xx})^2 \propto (\Delta u)^2 \propto \Delta F \propto (1/\Lambda)^2$, which indicates that $M_{xx} \propto 1/\Lambda$. This relation is in a reasonable agreement with the relationship observed experimentally, although the experimental values of M_{xx} increases slightly faster, *i.e.*, $M_{xx} \propto (1/\Lambda)^{1.3}$ (see Fig. 1c). Similarly, a tensile strain would drive the system away from its ground state to a higher energy state (see Fig. 4a). Therefore, a larger field-induced lattice

223 change could be generated, allowing the heterostructure to contract when E is applied
224 parallel to the (100) direction (Extended Data Fig. 5).
225
226 The electrostrictive effect is further confirmed by inspecting the response of local
227 distortions to the electric field. To describe the collective contribution of such local
228 distortions, we have extracted the electric dipoles induced by defects and the
229 displacements of cations and anions (Extended Data Fig. 6 and the Method part). Fig. 4d
230 presents the dipole distribution within the heterostructure (Λ = 4.65 nm) for ε^* = +0.05 at
231 300 K in the absence of an electric field. It is clear from this figure that various local
232 configurations exist, and there is no apparent ordered arrangement of local distortions. By
233 applying a large electrical field (E = 30 kV/cm) along the +x direction, the distribution of
234 electric dipoles becomes skewed in +x direction (Fig. 4e). This effect corresponds to a
235 more ordered structure with dipoles aligning along the external electric field.
236 Simultaneously, the density and magnitude of the dipoles increase substantially due to
237 the off-centre displacements of cation and anions. Fig. 4f summarises the normalized
238 probability distribution function, $P(\mu_x)$, against the normalized magnitude of the electric
239 dipole moments along the x-axis (μ_x) for heterostructures with different Λ under the same
240 tensile strain (ε^* = +0.05). With the absence of an electric field, the dipoles exhibit a broad
241 and symmetric distribution. This configuration gives rise to a zero macroscopic
242 polarisation (Fig. 4f solid line). However, applying an electric field along the +x direction

induces an asymmetric probability function with the peak in $P(\mu_x)$ shifted to higher values, demonstrating the alignment of the dipoles along the direction of the electrical field. With the decrease of Λ, the dipoles become less resistive to changes in the electrical field. Therefore, the alignment along the $+x$ direction is increasingly favoured. Such facile structural variations are responsible for increasing the change in energy and electrostrictive performance when decreasing the modulation length.

By engineering the electrostrictive materials with specifically designed interfaces, we demonstrated a significantly enhanced electrostriction coefficient surpassing any other known electrostrictive materials. These results produce a framework for engineering electrostrictive properties in heterostructures. It also offers new opportunities for designing and manipulating the performance of electrostrictive materials, e.g., for optical communications, which is at the heart of commercial technologies such as digital light-processing and optical switches and sensing and imaging devices with long-term stability. Unlike the toxic lead-based ferroelectrics such as PMN-PT and $MAPbI_3$, the current electrostrictive materials are environmentally friendly, making them suitable for a wide range of biomedical actuation and micro-sensors applications.

Online content

Any methods, additional references, Nature Research reporting summaries, source dats, extended data, supplementary information, aknowledgements, peer review information; details of author contributions and competing interesting; and statements of data and code availability are available at http://npg.nature.com

1. Ramesh, R. & Schlom, D. G. Creating emergent phenomena in oxide superlattices. *Nat. Rev. Mater*. **4**, 257-268 (2019).

2. Yang, M. M. Luo, Z., D. Zhao., J. Alexe, M., Piezoelectric and pyroelectric effects induced by interface polar symmetry. Nature. **584**, 377-381 (2020).

3. Li, F., Jin, L., Xu, Z. & Zhang, S. Electrostrictive effect in ferroelectrics: An alternative approach to improve piezoelectricity. *Appl. Phys. Rev*. **1**, 011103 (2014).

4. Kremer, F. et al. Giant lateral electrostriction in ferroelectric liquid-crystalline elastomers. *Nature*. **410**, 447-450 (2001).

5. Yimnirun, R., Moses, P. J., Newnham, R. E. & Meyer, R. J. Electrostrictive strain in low-permittivity dielectrics. *J. Electroceramics*. **8**, 87-98 (2002).

6. Li, F., Jin, L., Xu, Z., Wang, D. & Zhang, S. Electrostrictive effect in $Pb(Mg_{1/3}Nb_{2/3})O_3$-$xPbTiO_3$ crystals. *Appl. Phys. Lett*. **102**, 152910 (2013).

7. Zednik, R. J., Varatharajan, A., Oliver, M., Valanoor, N. & McIntyre, P. C. Mobile ferroelastic domain walls in nanocrystalline PZT films: The direct piezoelectric effect. *Adv. Funct. Mater*. **21**, 3104-3110 (2011).

8. Li, F. et al. Ultrahigh piezoelectricity in ferroelectric ceramics by design. *Nat. Mater*. **17**, 349-354 (2018).

9. Zhang, Q. M., Bharti, V. & Zhao, X. Giant electrostriction and relaxor ferroelectric behavior in electron-irradiated poly(vinylidene fluoride-trifluoroethylene) copolymer. *Science*. **280**, 2101-2104 (1998).

10. Korobko, R. et al. Giant electrostriction in Gd-doped ceria. *Adv. Mater*. **24**, 5857-5861 (2012).

11. Yavo, N. et al. Large Nonclassical Electrostriction in (Y, Nb)-Stabilized δ-Bi_2O_3. *Adv. Funct. Mater*. **26**, 1138-1142 (2016).

12. Cancellieri, C. et al. Electrostriction at the $LaAlO_3/SrTiO_3$ interface. *Phys. Rev. Lett*. **107**, 1–4 (2011).

13. Korobko, R. et al. In-situ extended X-ray absorption fine structure study of electrostriction in Gd doped ceria. *Appl. Phys. Lett*. **106**, 042904 (2015).

14. Hadad, M., Ashraf, H., Mohanty, G., Sandu, C. & Muralt, P. Key-features in processing and microstructure for achieving giant electrostriction in gadolinium doped ceria thin films. *Acta Mater*. **118**, 1-7 (2016).

15. Santucci, S., Zhang, H., Sanna, S., Pryds, N. & Esposito, V. Enhanced electromechanical coupling of $TiN/Ce_{0.8}Gd_{0.2}O_{1.9}$ thin film electrostrictor. *APL Mater*. **7**, 0-5 (2019).

16. Sata, N., Eberman, K., Eberl, K. & Maier, J. Mesoscopic fast ion conduction in nanometre-scale planar heterostructures. *Nature*. **408**, 946-949 (2000).

17. Domínguez, C. et al. Length scales of interfacial coupling between metal and insulator phases in oxides. *Nat. Mater*. **19**, 1182-1187 (2020).

18. Haeni, J. H. et al. Room-temperature ferroelectricity in strained $SrTiO_3$. *Nature*. **430**, 758-761 (2004).

19. Junquera, J. & Ghosez, P. Critical thickness for ferroelectricity in perovskite ultrathin films. *Nature*. **422**, 506-509 (2003).

20. Fong, D. D. et al. Ferroelectricity in ultrathin perovskite films. *Science*. **304**, 1650-1653 (2004).

21. B. K. Mani, C.-M. Chang, S. Lisenkov, and I. P. Critical Thickness for Antiferroelectricity in $PbZrO_3$. *Phys. Rev. Lett*. **097601**, 1-5 (2015).

22. Zhang, W. & Ouyang, J. Interface engineering of ferroelectric thin-film heterostructures. Nanostructures in Ferroelectric Films for Energy Applications: Domains, Grains, Interfaces and Engineering Methods (Elsevier Inc., 2019). doi:10.1016/B978-0-12-813856-4.00006-5

23. Ji, D. et al. Freestanding crystalline oxide perovskites down to the monolayer limit. *Nature*. **570**, 87-90 (2019).

24. Sanna, S. et al. Enhancement of the chemical stability in confined δ-Bi_2O_3. *Nat. Mater*. **14**, 500-504 (2015).

25. Sanna, S. et al. Structural instability and electrical properties in epitaxial Er_2O_3-stabilized Bi_2O_3 thin films. *Solid State Ionics*. **266**, 13-18 (2014).

26. Varenik, M. et al. Dopant concentration controls quasi-static electrostrictive strain response of ceria ceramics. *ACS Appl. Mater. Interfaces*. **12**, 39381-39387 (2020).

27. Li, Q. et al. Giant thermally-enhanced electrostriction and polar surface phase in $La_2Mo_2O_9$ oxygen ion conductors. *Phys. Rev. Mater*. **2**, 1-7 (2018).

28.Chen, B. et al. Large electrostrictive response in lead halide perovskites. *Nat. Mater*. **17**, 1020-1026 (2018).

Acknowledgements

This research was supported by the BioWings project funded by the European Union's Horizon 2020, Future and Emerging Technologies (FET) programme (Grant No. 801267) and Danish Council for Independent Research Technology and Production Sciences for the DFF- Research Project 2 (Grant No. 48293). N.P. acknowledges the funding from Villum Fonden for the NEED project (00027993) and Danish Council for Independent Research Technology and Production Sciences for the DFF- Research Project 3 (Grant No. 00069B). V.E. acknowledges the funding from Villum Fonden for the IRIDE project (00022862). N.G. and J.V. acknowledge funding from the GOA project "Solarpaint" of the University of Antwerp. The microscope used in this work was partly funded by the Hercules Fund from the Flemish Government. D.J. acknowledges funding from FWO Project G093417N from the Flemish fund for scientific research. D.C. acknowledge TOP/BOF funding of the University of Antwerp. This project has received funding from the European Union's Horizon 2020 Research Infrastructure - Integrating Activities for Advanced Communities under grant agreement No 823717-ESTEEM3. The authors would like to thanks Thierry Dèsirè Pomar for the English proofreading.

Author Contributions

H. Z., N. P. and V.E. conceived the idea and designed the project. H.Z. and S.S. prepared the samples and characterized the electromechanical properties. N.G. performed the STEM measurements and analyzed the STEM-EELS results. D.J. helped with the processing of the HAADF-STEM data analysis, and D.C. did the statistical analysis of

the EDX results under the supervision of N.G. and J.V. D.P. and R.D. performed the XRD and RSMs characterization. H. Z. and I. E.C. performed the atomic-scale simulations. D. V.C. performed the finite element simulations. H.Z. and N.P. wrote the manuscript with input from all the authors. All authors have read and agreed to the published version of the manuscript.

Competing interests The authors declare no competing financial interests.

Additional information

Supplementary information is available for this paper at www.nature.com.

Correspondence and requests for materials should be addressed to H. Z, V.E and N. P.

Reprints and permissions information is available online at http://npg.nature.com/reprintsandpermissions.

Methods

Thin-film fabrication. The heterostructures are fabricated by alternating CGO and ESB layers using pulsed laser deposition (PLD) with a multi-target carousel. The target-substrate distance was 50 mm. The 248 nm KrF excimer laser was operated at 2 Hz with a laser fluency of 1.8 J/cm^2. The deposition rate is ~0.05 nm per pulse. The total number of laser shots on the targets is 3560 (1780 for CGO and 1780 for ESB), giving rise to a total thickness of ~17 nm. The ratio of CGO and ESB is fixed at 1:1, whereas the thickness of each layer varies with modulation length. The deposition was performed at 600 °C at an oxygen partial pressure of 10^{-3} mbar. The heating/cooling rate is 10 °C/min. The Au top electrodes are sputtered with a Bal-Tec SCD 005 Sputter Coater at room temperature.

STEM, EDX and EELS measurement. The cross-section TEM lamellas were prepared via focused ion beam (FIB) using a FEI HELIOS 650 dual-beam Focused Ion Beam device. During the preparation process, carbon and platinum protective layers were deposited on top of the film. The aberration-corrected high angular annual dark-field scanning transmission electron microscopy (HAADF-STEM) and energy-dispersive X-ray spectroscopy (EDX) were performed on a probe aberration-corrected 'cubed' FEI TITAN 80-300 electron microscope operated at 300 kV equipped with SUPER-X EDX detector system. Line profiles of elemental distribution along the TEM lamellas were averaged over several unit cells laterally for better statistics. Electron energy loss spectroscopy (EELS) data were acquired on a double aberration-corrected 'cubed' FEI TITAN 80-300 electron microscope operated at 120 kV in monochromated mode, providing an energy resolution of 150 meV.

XRD and RSMs analysis. The crystal structure and the strain states were characterized by a high-resolution Bruker D8 discover diffractometer with monochromatic Cu $K_{\alpha 1}$ radiation (λ=1.5406 Å). The reciprocal space mappings were performed around the (221) asymmetric reflection of the NGO substrate.

Electrostriction measurements. The electrostriction properties of the NGO/CGO/$[ESB/CGO]_N$ heterostructures were measured with a planar electrode configuration, with the two electrodes placed on the top of the thin films in parallel (Fig. S4). This configuration avoids using the bottom electrode, thus facilitating the substrate's choice with desired lattice mismatch (and therefore biaxial strain).[29] The sinusoidal electric field was generated by AIM-TTI TGP 3100 function generator, amplified by a Trek 2220 amplifier. During the measurement, one end of the cantilever was clamped.

The oscillation of the free end was measured using a single-beam laser interferometer SIOS NA analyzer at the 2nd-harmonic of the electrical field. An Ametek 7230 DSP Lock-in Amplifier was used to improve the signal-noise ratio (down to 0.2 nm). Such a measuring configuration yields the longitudinal electrostriction coefficient (M_{13}) of the heterostructures (Extended Data Fig. 5a). However, M_{xx} is used for ease of comparison with results taken from the literature.

Atomic-scale simulations. Atomic-scale simulations were performed based on the well-established classical simulation approach to model the various possible distributions of the point defects within the heterostructures. The interatomic interactions are described by:

$$V_{ij} = \frac{Z_i Z_j}{4\pi\varepsilon_0 r_{ij}} + A_{ij}\exp\left(-\frac{r_{ij}}{\rho_{ij}}\right) - \frac{C_{ij}}{r_{ij}^6}$$

where the first term describes the long-range Columb interactions, and the following two terms correspond to the short-range electron cloud overlap and dispersions, respectively. The parameters, r_{ij}, $Z_{i(j)}$ and ε_0 are the distance between ions *i* and *j*, the ion's valences, the permittivity of free space, respectively. A_{ij}, ρ_{ij} and C_{ij} are the empirical Buckingham parameters (listed in Extended Data Fig. 7a).

The molecular dynamics (MD) were performed with the following steps: 1) Construct the (100)×(0$\bar{1}$1)×(011)-orientated heterostructures with various modulation length; 2) Introduce the dopants and oxygen vacancies at random; 3) Apply biaxial strains by adjusting the in-plane lattice parameters to specific values; 4) Equilibrate the structures

410 at 2400 K for 600 ps, followed by another equilibration at 300 K for 300 ps; 5) Turn on
411 the electrical field along the (100)-crystallographic direction at 300 K and extract the
412 optimized structures and free energies after 100 ps. During the simulations, the in-plane
413 lattices parameters are fixed, whilst the out-of-plane lattice parameters are free to relax.
414 The pressure was kept constant (1.01 mbar), and the temperature was monitored by a
415 Nosé-Hoover thermostat (*NPT* ensemble),[30,31] as implemented in the LAMMPS package.[32]
416 Large supercells of $10 \times 8\sqrt{2} \times 24\sqrt{2}$ (41472 atoms) and $16 \times 12\sqrt{2} \times 12\sqrt{2}$ (49768
417 atoms) were used to model the interfacial coupling (Fig. 3) and the modulation length and
418 strain (Fig. 4), respectively.

419 The electronic dipoles were calculated to describe the local distortions and their
420 response to the electric field. The analysis was realized by dividing the period simulation
421 box into $N \times N \times N$ cubes, where the side length of each cube is $L_{cube} = L_{box}/N$. For
422 visualizing and statisting of the dipoles, the period simulation box was divided into 4 × 4
423 × 4 and 8 × 8 × 8 cubes, respectively. By summing the point charges within the *i*th cube,
424 the net positive charge (q_i^+) and negative charge (q_i^-) and the distance ($\vec{r}_i$) between q_i^+
425 and q_i^- were determined. The dipole moment was then calculated by $\vec{\mu}_i = q_i\vec{r}_i$, the
426 direction of which is parallel to the vector pointing from q_i^- to q_i^+ in the *i*th cube.
427 Extended Data Fig. 8 schematically illustrated the appearance of electronic dipoles
428 induced by the defects within CeO_2 and δ-Bi_2O_3.
429

Data Avalibility

The data that support the findings of this study are available from the corresponding authors upon reasonable request.

29. Nigon, R., Raeder, T. M. & Muralt, P. Characterization methodology for lead zirconate titanate thin films with interdigitated electrode structures. *J. Appl. Phys*. **121**, 204101 (2017).

30. Nosé, S. A unified formulation of the constant temperature molecular dynamics methods. *J. Chem. Phys*. **81**, 511-519 (1984).

31. William G. Hoover. Canonical dynamics: Equilibrium phase-space distributions William. *Phys. Rev. A*. **31**, 1695-1697 (1985).

32. Plimpton, S. Fast Parallel Algorithms for Short-Range Molecular Dynamics. *J. Comput. Phys*. **117**, 1-19 (1995).

Figure legends:

Figure 1

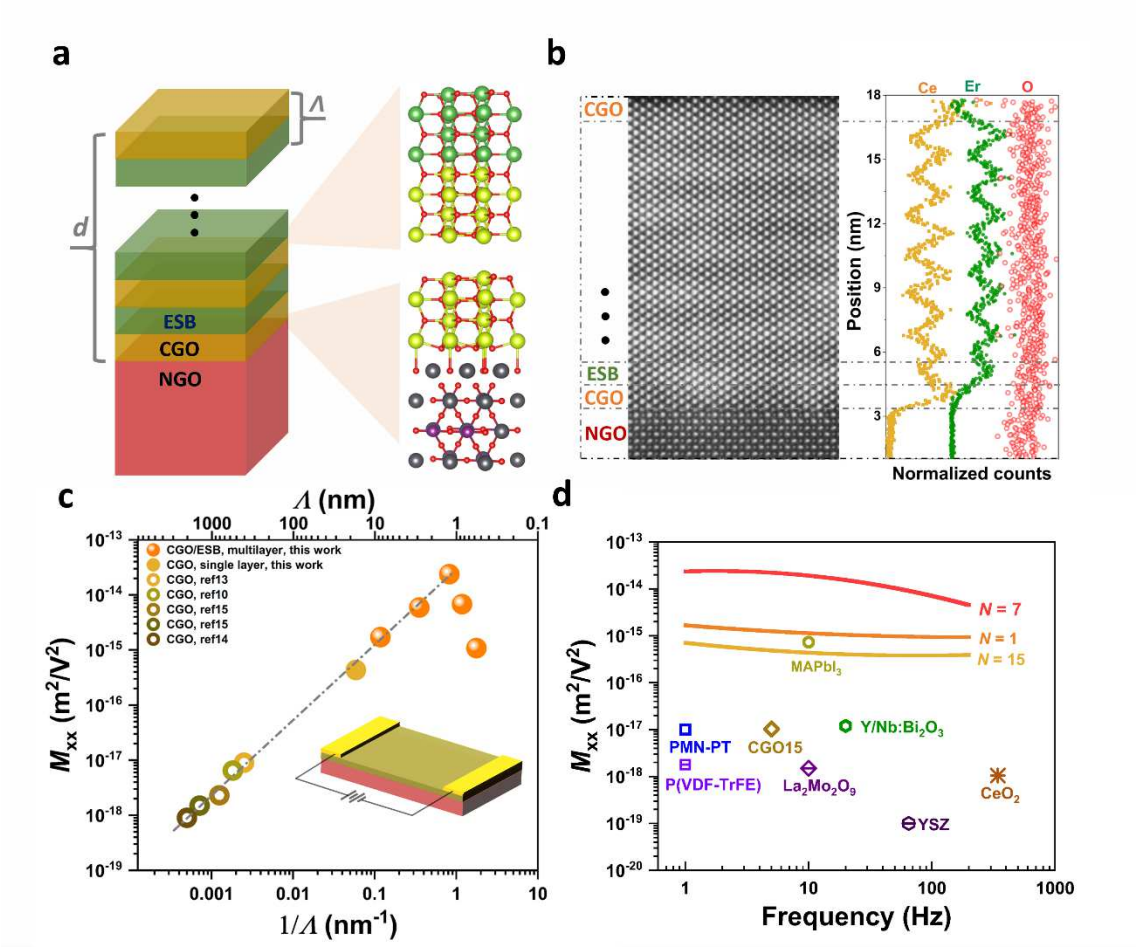

Fig. 1| Multilayer structure and electrostrictive property of NGO/CGO/[ESB/CGO]$_N$. a, Schematic illustration of the multilayer architecture. **b**, STEM-HAADF image and EDX compositional variations for $N = 7$. **c**, Electrostriction coefficient (M_{xx}) as a function of modulation length (Λ) measured at 1 Hz. For single layered films, Λ is the total thickness. The inset schematically illustrate the top-top electrode configuration. **d**, Electrostriction coefficient (M_{xx}) as a function of frequency for heterostructures with $N = 1$, 7 and 15. Electrostriction properties of various electrostrictive materials are shown for comparison: CeO_2,[26] CGO15,[26] Y/Nb:Bi_2O_3,[11] YSZ,[11] $La_2Mo_2O_9$,[27] PMN-PT,[6] P(VDF-TrFE),[9] and $MAPbI_3$.[28]

Figure 2

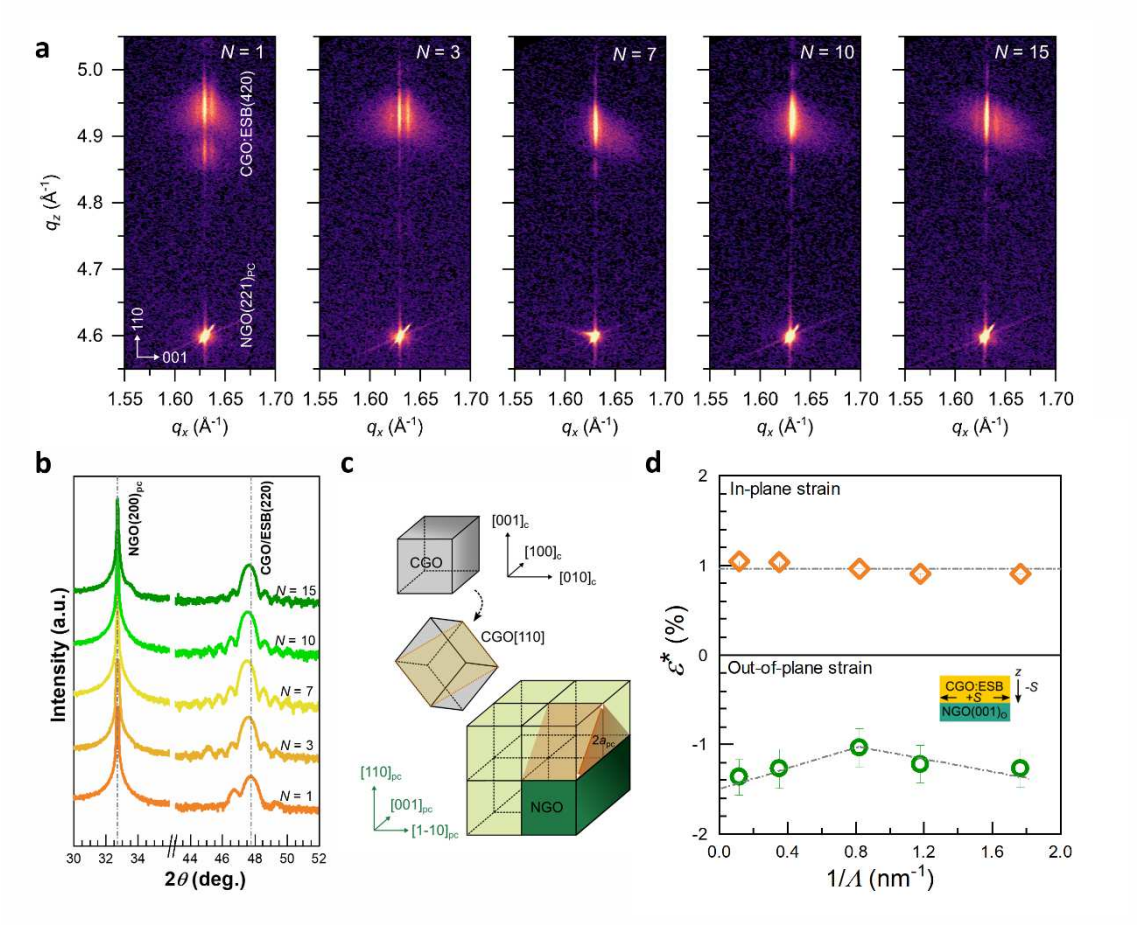

Fig. 2| Structure analysis for NGO/CGO/[ESB/CGO]$_N$. **a**, Reciprocal space mappings (RSMs) of the NGO/CGO/[ESB/CGO]$_N$ heterostructures around the asymmetric $(221)_{pc}$ reflection of the NGO substrate. **b**, X-ray diffraction pattern (2θ-ω scans) of the films. **c**, Schematic illustration of the epitaxial relationship of the heterostructure with respect to the NGO substrate. **d**, the evolution of the in-plane and out-of-plane strains. The in-plane and out-of-plane strains are calculated based on the RSMs and 2θ-ω scans, respectively. The error bars in **d** represent the fitting error of the lattice constants.

Figure 3

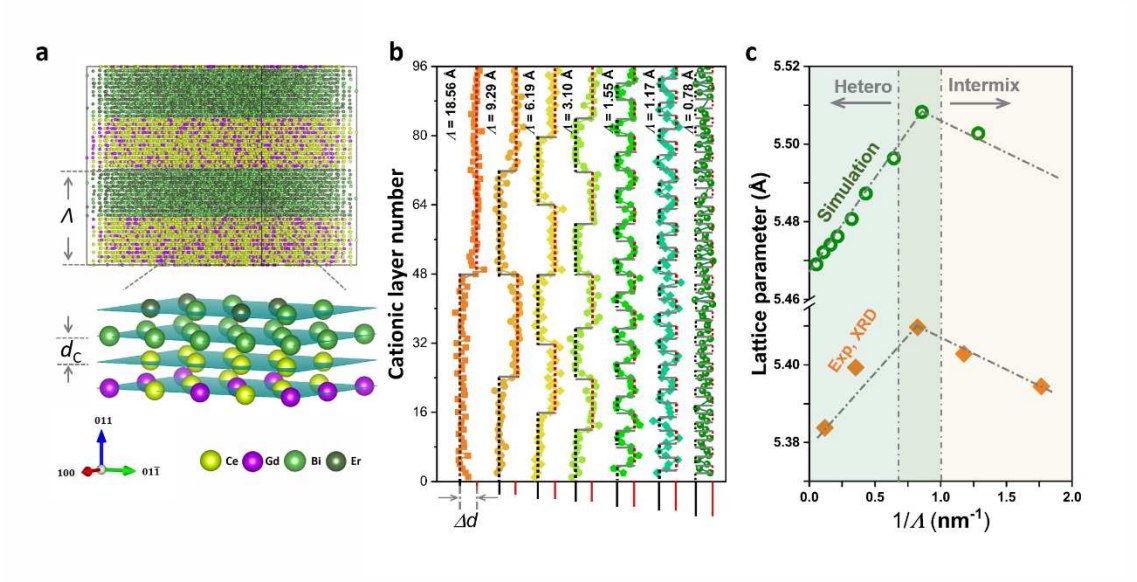

Fig. 3| Mechanism of interlayer interaction. **a**, Schematic illustration of the modulation length (Λ) and the cationic interplanar distance (d_C) for heterostructures. The oxygen ions are omitted for clarity. **b**, The variation of d_C as a function of Λ projected onto the out-of-plane direction. The dark and red dot lines represent the individual interplanar distances of CGO (1.92 Å) and ESB (1.96 Å), respectively. Δd is 0.04 Å. **c**, variation of out-of-plane lattice parameters as a function of Λ. The dash-dotted line is guided to the eyes only.

Figure 4

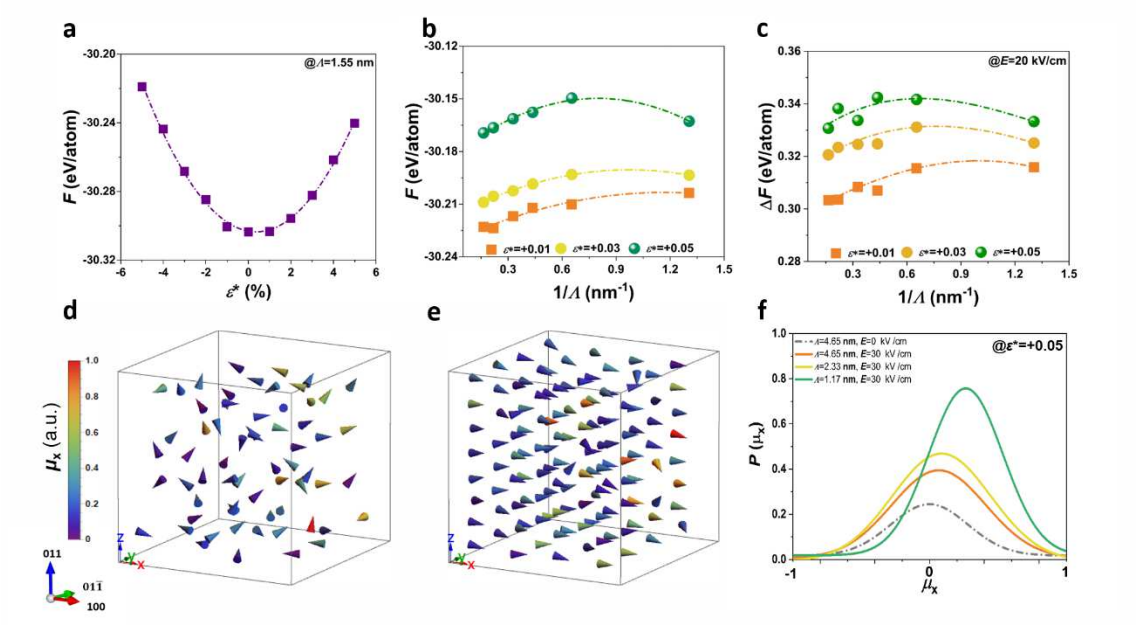

Fig. 4| Mechanism of the enhanced electromechanical response. **a**. Free energy (F) for heterostructure with a modulation length (Λ) of 1.55 nm (8 cationic layers). **b**. Free energy as a function of Λ with different biaxial strains (ε*). **c**. Free energy change (ΔF) after applying electric field (E) **d and e,** The distribution of dipoles within the heterostructure ($1/\Lambda$ = 0.22 nm^{-1}) for E = 0 (**d**) and 30 kV/cm (**e**) along the +x direction. **f**. Normalized probability distribution functions, $P(\mu_x)$ against the normalized dipole moment along the x-axis (μ_x) for heterostructures with different Λ under the same tensile strain (ε* = +0.05). The dash-dotted lines in **a**, **b** and **c** are parabolic fitting to the calculated results.

Supplementary Files

This is a list of supplementary files associated with this preprint. Click to download.

- AtomicallyengineeredinterfacesyieldextraordinaryelectrostrictionsupplemetaryInformation.pdf
- AtomicallyengineeredinterfacesyieldextraordinaryelectrostrictionExtendedData.pdf